SOFT ROBOTS

A hyperelastic torque-reversal mechanism for soft joints with compression-responsive transient bistability

Woo-Young Choi[1,2]†, Woongbae Kim[3,4]†, Jae-Ryeong Choi[1], Sung Yol Yu[1], Seunguk Moon[1], Yong-Jai Park[5], Kyu-Jin Cho[1]*

Snap-through, a rapid transition of a system from an equilibrium state to a nonadjacent equilibrium state, is a valuable design element of soft devices for converting a monolithic stimulus into systematic responses with impulsive motions. A common way to benefit from snap-through is to embody it within structures and materials, such as bistable structures. Torque-reversal mechanisms discovered in nature, which harness snap-through instability via muscular forces, may have comparative advantages. However, the current intricacy of artificial torque-reversal mechanisms, which require sophisticated kinematics/kinetics, constrains design possibilities for soft joints and devices. Here, we harnessed hyperelasticity to implement a torque-reversal mechanism in a soft joint, generating repetitive cilia-like beating motions through an embedded tendon. The developed hyperelastic torque-reversal mechanism (HeTRM) exhibits transient bistability under a specific compressive displacement/force threshold, with snap-through occurring at the point where the transience ends. To validate the effectiveness of this design principle, we explored the functionalities of HeTRM in energy storage and release, dual modes for impulsive and continuous motion, mechanical fuse, and rapid three-dimensional motions, through proof-of-concept soft machines. We expect that this design principle provides insight into incorporating snap-through behavior in soft machines and may aid in understanding the relationship between torque-reversal mechanisms and bistability.

INTRODUCTION

In many natural and artificial systems, a soft body serves as a medium capable of converting various types of monolithic stimuli—such as mechanical (*1*, *2*), fluidic (*3*–*7*), electric (*8*–*10*), magnetic (*11*, *12*), thermal (*13*, *14*), and humidity-related (*15*) stimuli—into systematic, adaptive, and lifelike responses. However, compared with rigid components, soft bodies are typically considered less suitable for producing fast and powerful motion. Research aimed at overcoming this issue through actuation methods has shown promising results with combustion-driven (*16*–*18*) and electrohydraulic-driven approaches (*19*, *20*).

Leveraging snap-through, a rapid transition of a system from an equilibrium state to a nonadjacent equilibrium state, is another widely adopted approach for achieving impulsive motion (*21*–*23*). Snap-through instabilities are typically exploited through material properties, structural designs, or topological configurations, characterized by a nonlinear load-displacement relationship with an intermediate region of negative stiffness (*21*). For example, hyperelastic spherical membranes, which soften and then stiffen under volumetric expansion, allow researchers to harness snap-through instability via fluidic (*24*, *25*) or electric (*26*) actuation for high-speed soft machines (*24*, *25*) and jumping mechanisms (*27*). Another common approach involves compliant mechanisms. Bending spines with springs at both ends, for instance, exhibit snap-through behavior during flexion and extension, enabling high-speed galloping (*28*) and reconfiguration (*29*) of soft robots. Topological designs, such as constrained elastic beams, curved plates, and invertible shells, are also used to embody snap-through instability in soft or flexible structures (*21*). Constrained elastic beams, with their simple structure generating rapid back-and-forth motion, have been used in soft devices for both terrestrial and aquatic propulsion (*30*, *31*). Curved plates, as demonstrated in nature by Venus flytrap leaves rapidly transforming from convex to concave to catch prey (*32*), are often used as fast and energy-efficient soft grippers (*33*–*35*). Invertible shells can be easily designed into enclosed geometries for fluid-driven soft devices, such as jumping robots and valves (*27*, *36*). These topological designs can exhibit either bistability or monostability, both with snap-through instability, depending on the tuning of their geometric parameters (*21*, *36*–*39*). Therefore, for their bidirectional snapping motion, users can selectively choose functionalities between storing and releasing potential energy through antagonistic actuation (bistability) or restoring the initial shape by simply adjusting the level of unidirectional actuation (monostability) (fig. S1).

The jumping by fleas (*40*, *41*) and the ultrafast striking of stomatopods (mantis shrimp) (*42*–*44*) are other intriguing biological examples of impulsive motions using snap-through instability. These systems store energy by compressing muscles and then release it by reversing the direction of the torque, a process known as the torque-reversal mechanism. Figure 1A shows the simplified compliant mechanism of a flea's torque-reversal mechanism for jumping, and Fig. 1B illustrates changes in joint angle and potential energy relative to the spring displacement (corresponding to the contraction of the flea's extensor muscle) in the system. First, the joint is latched, and the spring stores energy [Fig. 1, A and B, (i) and (ii)]. Subsequently, a triggering force (corresponding to the flea's triggering muscle)

[1]Biorobotics Laboratory, Soft Robotics Research Center, Institute of Advanced Machines and Design, Department of Mechanical Engineering, Institute of Engineering, Seoul National University, Seoul, Republic of Korea. [2]NAVER LABS Corp., Seongnam-si, Gyeonggi-do, Republic of Korea. [3]Center for Humanoid Research, Artificial Intelligence and Robotics Institute, Korea Institute of Science and Technology (KIST), Seoul, Republic of Korea. [4]Korea Institute of Science and Technology Europe (KIST-EUROPE), 66123 Saarbrücken, Germany. [5]Department of Mechatronics Engineering, Kangwon National University, Chuncheon-si, Gangwon-do, Republic of Korea.
*Corresponding author. Email: kjcho@snu.ac.kr
†These authors contributed equally to this work.

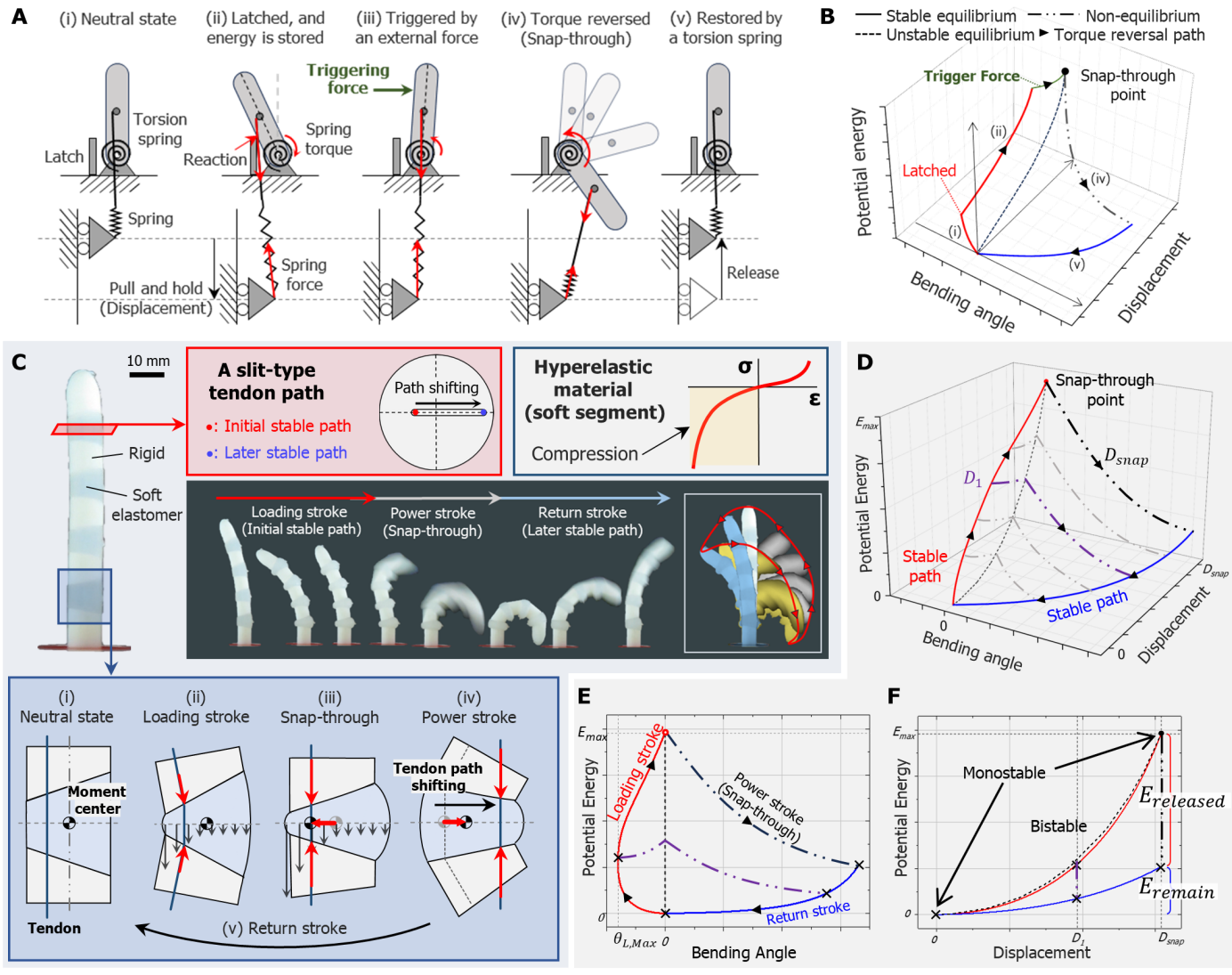

Fig. 1. Torque-reversal mechanism and HeTRM. (**A**) A linkage-based torque-reversal mechanism, mimicking the flea's jumping leg. (**B**) Joint angle and potential energy of the linkage-based torque-reversal mechanism relative to the spring displacement. (**C**) Design and principle of the HeTRM. A HeTRM beam was composed of alternating rigid (VeroWhite, Stratasys) and hyperelastic soft (Ecoflex 00-30, Smooth-On, Inc.) segments. (Red inset) The cross section of the joint features a slit-type tendon path, which allows for lateral shifting of the tendon between the initial stable path and the later stable path. (Dark inset) In the HeTRM beam, energy was stored during the loading stroke and then released during the power stroke, resulting in a cilia-like bending motion. The remaining energy was used for the restoration to the original position. (Blue inset) Schematic showing torque reversal and tendon movement in the HeTRM cycle due to internal stress distribution within the soft joint. (**D**) Joint angle and potential energy of the HeTRM relative to the tendon displacement. (**E**) Potential energy as a function of bending angle. (**F**) Potential energy as a function of displacement, illustrating the released and remaining energy of the HeTRM.

slightly rotates the joint in another direction, reversing the direction of the torque, and then the stored energy is rapidly converted into rotational motion [Fig. 1, A and B, (iii) and (iv)]. Upon releasing the spring, the system returns to its initial state, allowing the cycle to be repeated [Fig. 1, A and B, (v)].

The behavior of the torque-reversal mechanism is nonreciprocal, as depicted in Fig. 1B, where the trajectory during the initial energy-loading phase and the trajectory after snap-through define two distinct stable equilibrium paths. This feature is distinct from bistable structures where the snap-through instability is determined by the structural design and indicates that several functionalities can be achieved. First, the amount of energy released during snap-through can be controlled via active triggering, using the feature that greater contraction force or displacement leads to greater stored energy. Second, cyclic energy storage and release behavior can be generated by repeating the contraction, trigger, and release. Linkage configurations can be designed for torque reversal to be self-triggered with a single contraction actuator, as seen in the water-strider robot's jumping mechanism (*41*) and the mantis shrimp–inspired mechanism (*44*), making the trigger actuator unnecessary unless energy release control is required. Third, general continuous motion without snap-through can be selectively used by applying the initial compressive force at the opposite side of the rotational center (in other words, fleas can continuously move their legs to crawl instead

of jumping). However, the current design rule for torque-reversal mechanisms, which requires a sophisticated kinetics/kinematics design incorporating mechanical latch and spring components, has consequently resulted in only a few reported design methods based on *n*-bar linkage structures, to the best of our knowledge. The resulting incompatibility with soft joints precludes the use of torque-reversal mechanisms in the promising field of soft-bodied systems and soft robotics.

This paper introduces a design method for a torque-reversal mechanism embodied in soft joints, enabling a repetitive, cilia-like beating motion by simply pulling a single tendon. The proposed mechanism, named the hyperelastic torque-reversal mechanism (HeTRM), operates by gradually storing energy in the soft joints and then self-triggers a snap-through motion that rapidly releases the stored energy. We analyzed the HeTRM and found that the system exhibits bistability for compressive forces below a certain critical value. However, as the compressive force surpasses this critical value, one of the stable states dissipates, causing the system to become monostable and resulting in snap-through instability. This behavior is attributed to self-stress dispersion within the soft joints because of their hyperelastic material properties, leading to localized stiffness changes. Through modeling and experiments on the HeTRM, we preprogrammed the snap-through point and controlled the amount of energy stored and released via self-triggering. Furthermore, we experimentally validated the concept of the HeTRM's active energy storage and release functions using a triggering tendon. We demonstrated various HeTRM applications, including an artificial metachronal rhythm, an egg cracker, a dual-mode soft gripper, a mechanical fuse, a rapidly twisting tentacle-like gripper, and a crawler with out-of-plane spatial motion, to showcase its potential in soft body systems.

RESULTS

Inspiration from the beating motion of cilia

A noteworthy example of nature producing fast and dynamic motion with soft joints is the beating motion of cilia (*12*, *45*, *46*). At rest, the cilium is a flexible beam with no structural bias. However, during the beating motion, one side of dyneins' arms is actuated while the other side is inactive, making the bending shape structurally stable (*45*). By bilaterally switching between stable bending geometries, cilia cyclically generate power and recovery strokes that produce microfluidic thrust to convey substances or move the host cell's body. This behavior served as an inspiration for incorporating snap-through motion into soft joints without the need for geometrical complexity and inherent structural bistability.

A self-triggered HeTRM

To leverage the torque-reversal mechanism into soft joints, we placed soft hyperelastic material segments between rigid segments and embedded a single tendon as shown in Fig. 1C. We designed the segments to be in an inclined shape (a trapezoidal shape in lateral view) and a slit-type tendon path, a cross-sectionally narrow and hollow area of both the rigid and soft segments, allowing for lateral movement of the tendon (red inset figure in Fig. 1C). We illustrated a single cycle of the unit HeTRM beam schematically in Fig. 1C (blue inset). At the neutral state, the embedded tendon was positioned at the narrower side of the soft segment [Fig. 1C(i)]. When we pulled the tendon, the soft joint condensed and the beam bent [Fig. 1C(ii)]. Because of the hyperelasticity of the soft material, where the stiffness rapidly increased as the material was compressed (fig. S2), the larger strain in the narrow side compared with that of the wide side caused a sharp stiffness difference between these two regions. This phenomenon changed the distribution of internal stress as the applied tension increased, causing the moment center of the structure to gradually shift toward the position of the tendon. Our computational results for the moment of force (i.e., torque) revealed that the effect of increasing tension initially outweighed the effect of moment arm shortening; however, this relationship reversed at a later stage (fig. S3 and Supplementary Methods). Therefore, during this loading stroke phase, the bending angle reached a local peak and then decreased toward 0°. When the tendon was pulled to the critical displacement or tension, the torque eventually reversed [Fig. 1C(iii)]. This torque reversal (i.e., snap-through) caused the HeTRM beam to produce a rapid and dynamic power stroke in the opposite bending direction as the tendon quickly slid to the other end of the slit-type tendon path [Fig. 1C(iv)]. Last, when we released the tendon, the system returned to its initial state [Fig. 1C(v)]. The cyclical motion of the self-triggered HeTRM resembled the power stroke and return stroke of the ciliary beating motion, as demonstrated with a four–soft segment HeTRM beam in Fig. 1C (black inset), fig. S4, and movie S1.

Compression-responsive transient bistability of HeTRM

The HeTRM beam, when slightly bent by pulling the tendon, exhibited bistability; it could transition to a stable configuration in the opposite direction if an external force was applied to push the tip. However, when the tendon was pulled beyond the critical displacement, causing a self-triggered snap-through, the HeTRM beam became monostable in its bent configuration (as demonstrated in movie S2). To investigate this compression-responsive transient bistability, we visualized the modeling results in Fig. 1D(i), showing the relationship between the tendon displacement (D), the potential energy (E), and the bending angle of the beam (θ) (see details in table S1). The red line in Fig. 1D(i) indicates the model-based computational result when the tendon was pulled from its initial position, generating the loading stroke. The blue line indicates the computational result when the tendon was released after the torque reversal was triggered, i.e., when the tendon was at the opposite end of the tendon slit compared with its initial position. The black dashed line represents the computational result for a hypothetical situation in which the HeTRM beam did not bend, indicating the unstable equilibrium points for the corresponding tendon displacements. Figure 1E shows that the HeTRM beam was bistable for the critical displacement, D_{Snap}. For example, D_1, indicated by the purple dash-dotted lines in Fig. 1, had two stable points: one on the red line and another on the blue line. The HeTRM system could switch between these two stable points via snap-through if an external force was exerted to deform the HeTRM beam to the corresponding unstable equilibrium point on the black line. At this point, the energy difference between the unstable equilibrium point and the corresponding stable point represented the energy stored or released, depending on the snap-through direction.

For the points on the red line (the loading stroke), the system exhibited a negative peak value of the bending angle. After this point, the bending angle was restored, and the system intersected the black dashed line at D_{Snap}. Because the intersecting point was an unstable equilibrium point, the stability on the red line vanished

from this point of intersection ($\geq D_{Snap}$), and the HeTRM system transitioned from bistable to monostable. This compression-responsive transient bistability explained the self-triggering snap-through behavior of the HeTRM, a system transition from the disappearing stable point to the remaining stable point. When the tendon was pulled, the HeTRM beam deformed along the initial stable path and stored energy in the soft joint (red line). Then, when the system reached the critical point where bistability ends, it rapidly transitioned into the remaining stable state on the blue line and released energy equal to the difference in energy between the two points ($E_{released}$ in Fig. 1F). Last, when the tendon was released, the HeTRM system used the remaining energy (E_{remain}, Fig. 1F) as a restoring force and returned to the origin along the blue line.

The compression-responsive transient bistability offered several functionalities. First, we could simply achieve repetitive and continuous cilia-like impulsive motion by repeatedly controlling displacement from 0 to D_{Snap} and back to 0. Second, we could selectively implement continuous bending by placing another tendon at the opposite end of the slit (positioned at the wider side of the soft segment). When this tendon was pulled from the neutral state of the HeTRM beam, the beam repeatedly bent and unbent in one direction following the stable path corresponding to the blue line (implemented as a normal mode in the following "Dual-mode HeTRM soft gripper" section). Third, we could actively control the amount of energy released using an additional actuator for triggering (detailed in the "Active triggering of HeTRM" section). Fourth, we could mechanically constrain the HeTRM beam to perform the intended function only at input levels below the critical point (detailed in the "HeTRM soft mechanical fuses for safe interaction" section).

Parametric study for HeTRM

To better understand the HeTRM, we investigated the design parameters of the soft joint through modeling and experiments. The design parameters included the joint inclination angle (α), the joint center height (h_C), the distance from the center to the tendon position during the loading stroke (d_L), and the distance from the center to the tendon position during the return stroke (d_R), as illustrated in Fig. 2A. The model-based computational results for each parameter are shown in Fig. 2 (B to F). Detailed numerical values from the model and experimental results for the varying parameters are presented in Fig. 2 (G to I) and tables S2 to S4.

As shown in Fig. 2B, increasing α resulted in the HeTRM storing more potential energy for the same tendon displacement during the loading stroke. Conversely, during the return stroke, the HeTRM stored less energy for the same tendon displacement. Consequently, the efficiency of released energy relative to stored energy ($\eta_{out} = E_{released} / E_{stored}$) increased with increasing α. However, increasing α caused the snap-through to occur at a lower triggering displacement ($D_{Trigger}$) and tension force ($F_{Trigger}$), resulting in decreased E_{stored} and $E_{released}$. This indicates that α acted as an amplifier for the distortion of the internal stress distribution during compression, making the HeTRM more effective and easier to trigger, as illustrated by the experimental and modeling results in Fig. 2G and table S2.

As shown in Fig. 2C, increasing h_C resulted in storing less energy for the same D in both the loading and return strokes, which contrasts with varying α where the trend was opposite for the two strokes. Furthermore, with increasing h_C, the snap-through was triggered at a larger D and released considerably more energy but with a slight decrease in efficiency. The experimental and computational results in Fig. 2H and table S3 show that both the input values for triggering and the energy values progressively increase with increasing h_C. Overall, increasing h_C was analogous to increasing the capacity of the HeTRM.

The model-based computational results for varying design parameters of the tendon slit are shown in Fig. 2D for d_L and in Fig. 2E for d_R. As d_L increased, snap-through occurred for larger D, and therefore, all energy values also increased, as supported by both experimental and computational results in Fig. 2I and table S4. Meanwhile, increasing d_R reduced the remaining energy in the return strokes (E_{return}), both of which changed substantially. Figure 2F shows the snap-through points for varying d_L on the black dashed line and the later stable paths for varying d_R, demonstrating that d_L and d_R determined the amount of energy stored and released, respectively, for the given geometry of HeTRM.

Figure 2 (G to I) shows the model-based computational and experimental values of displacement, tension, and released energy at the point of self-triggering. For $D_{Trigger}$ and $E_{released}$, the experimental results for eight of the nine parameters fell within the target design error range of the 95% confidence interval. The exception was for $d_L = 0.9$ mm, which matched the modeling result for $d_L = 0.8$ mm; we suspected that manufacturing tolerances and tendon thickness contributed to this discrepancy. For the triggering tension ($F_{Trigger}$), four of the nine parameters matched the model predictions within the error range, which was reasonable given the unaccounted factors, such as shear force and friction.

On the other hand, E_{stored} and E_{return} were higher in the experimental data compared with the computational values, resulting in the actual energy efficiency being roughly 15 to 20% lower than that calculated by the model (tables S2 to S4). We suspected that this discrepancy arose because the experimental energy values were calculated from the tension-displacement loop, where shear force and friction, factors not accounted for in our simplified model, caused differences, in particular in regions with large bending angles. This is supported by fig. S5, which shows that the tension differences between the model and the experiments increased and then decreased as the tendon was pulled, suggesting a reduced influence of shear force and friction at smaller bending angles. We also inferred that the model's reasonable agreement with experimental results for $E_{released}$, calculated by the difference between E_{stored} and E_{return}, was due to the counteraction of the unconsidered factors, although this requires further investigation.

HeTRM-based metachronal rhythm and impulsive actuation

A metachronal rhythm is a representative behavior of cilia structured in a longitudinal row, generated by their sequential actions with a certain phase difference between adjacent neighbors (*46*). Through the generation of traveling waves, this metachronal rhythm enables the transportation of fluids and particles or the locomotion of living systems (*12*). We used the modeling result (as h_C increases, D_{snap} increases proportionally; fig. S6) to artificially mimic the metachronal rhythm, as shown in Fig. 3A and movie S3. Five HeTRM structures differing only in their h_C values by 1 mm were placed in a row ($h_C = 9$ mm on the left and $h_C = 13$ mm on the right, with D_{snap} predicted to increase proportionally by an interval of 0.895 mm). The tendons, routed through Bowden cables, were connected to a single pulley to ensure the same tendon displacements when a motor was driven. As a result, the HeTRM beams were sequentially

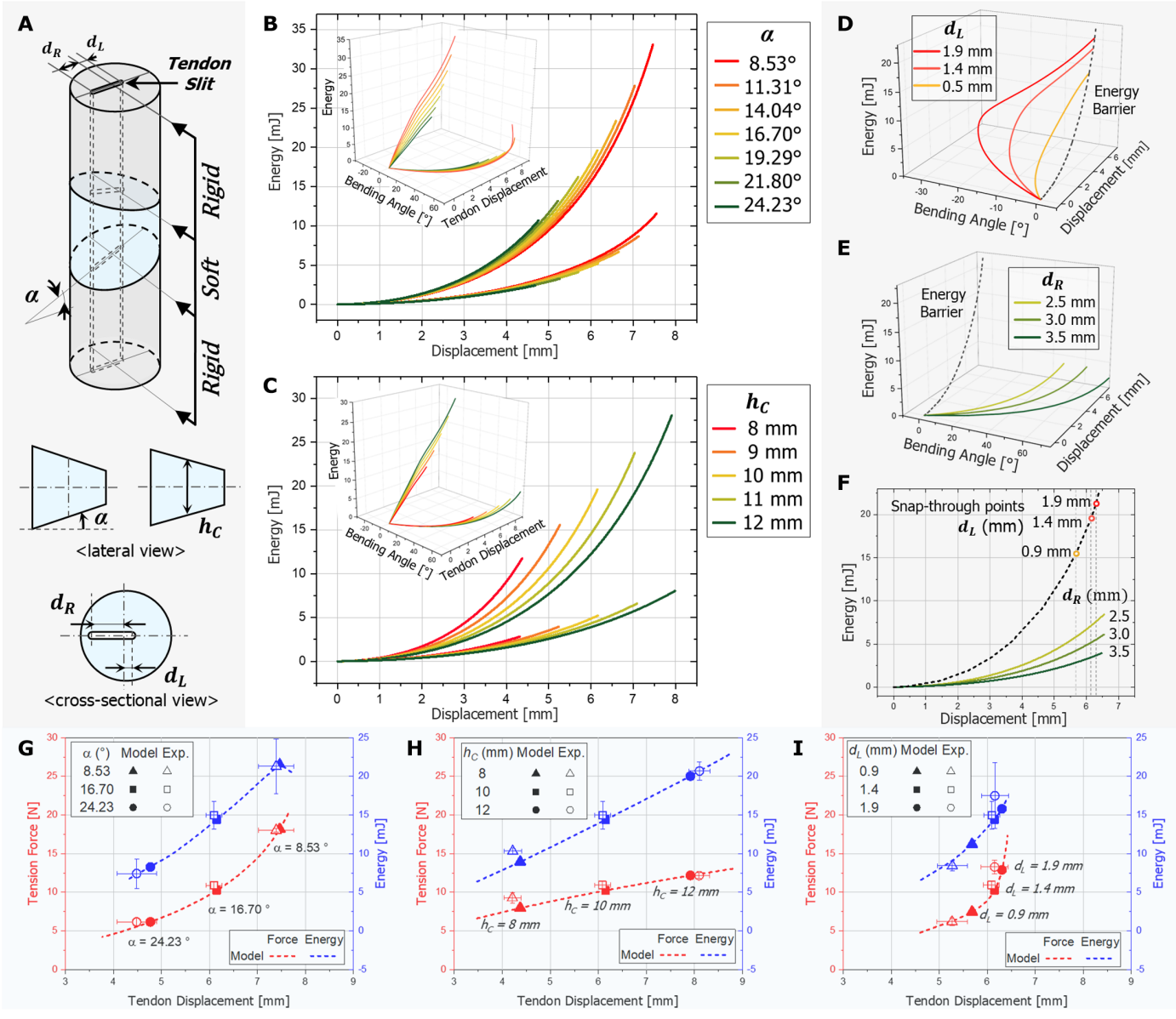

Fig. 2. Characterization of the HeTRM through modeling and experiments. (**A**) Schematic representation of the HeTRM showing key design parameters. Modeling results for (**B**) the design parameter of the soft joint inclination angle (α) and (**C**) the joint center height (h_C). Modeling results for (**D**) the slit-type tendon path parameter, d_L, and (**E**) d_R. (**F**) Snap-through points for varying d_L and the return paths with varying d_R values. (**G**) Comparison of the modeling and experimental results for the design parameter α, (**H**) h_C, and (**I**) d_L. Trends predicted by the modeling are indicated with dashed lines. Tendon displacement, tension, and released energy between the experiments and the model for specific design variables were compared.

triggered one by one from left to right by driving a single motor, generating the artificial metachronal rhythm.

The self-triggered HeTRM beam stored energy gradually from the actuator and then released it impulsively, whereas a typical soft bending joint would require direct impulsive energy transfer from the actuator for equivalent function. To showcase this functionality, we conducted an eggshell-cracking challenge with a single-joint HeTRM beam that can selectively operate a HeTRM mode (energy storage and release swing motion) and a normal mode (continuous bending motion). Those modes were achieved by placing two tendons at both ends of the tendon slit and selectively pulling each tendon (Fig. 3B and movie S4). When the tendon for the HeTRM mode was pulled at 4 mm/s by a motor-tendon system, the beam hit the egg as the HeTRM was triggered, making a "click" sound and creating an oval-shaped crack at the first strike. In contrast, with the same tendon displacement control in the normal mode, the tip of the beam slid along the surface of the egg, then rotated as the structure collapsed, failing to transmit enough force to crack the surface of the egg. The experimental result for tendon displacement and tension for the HeTRM mode is shown in Fig. 3C. At a stored energy of 67.05 mJ, snap-through occurred and 42.86 mJ was released, which was notably greater than the 13- to 26-mJ range required to

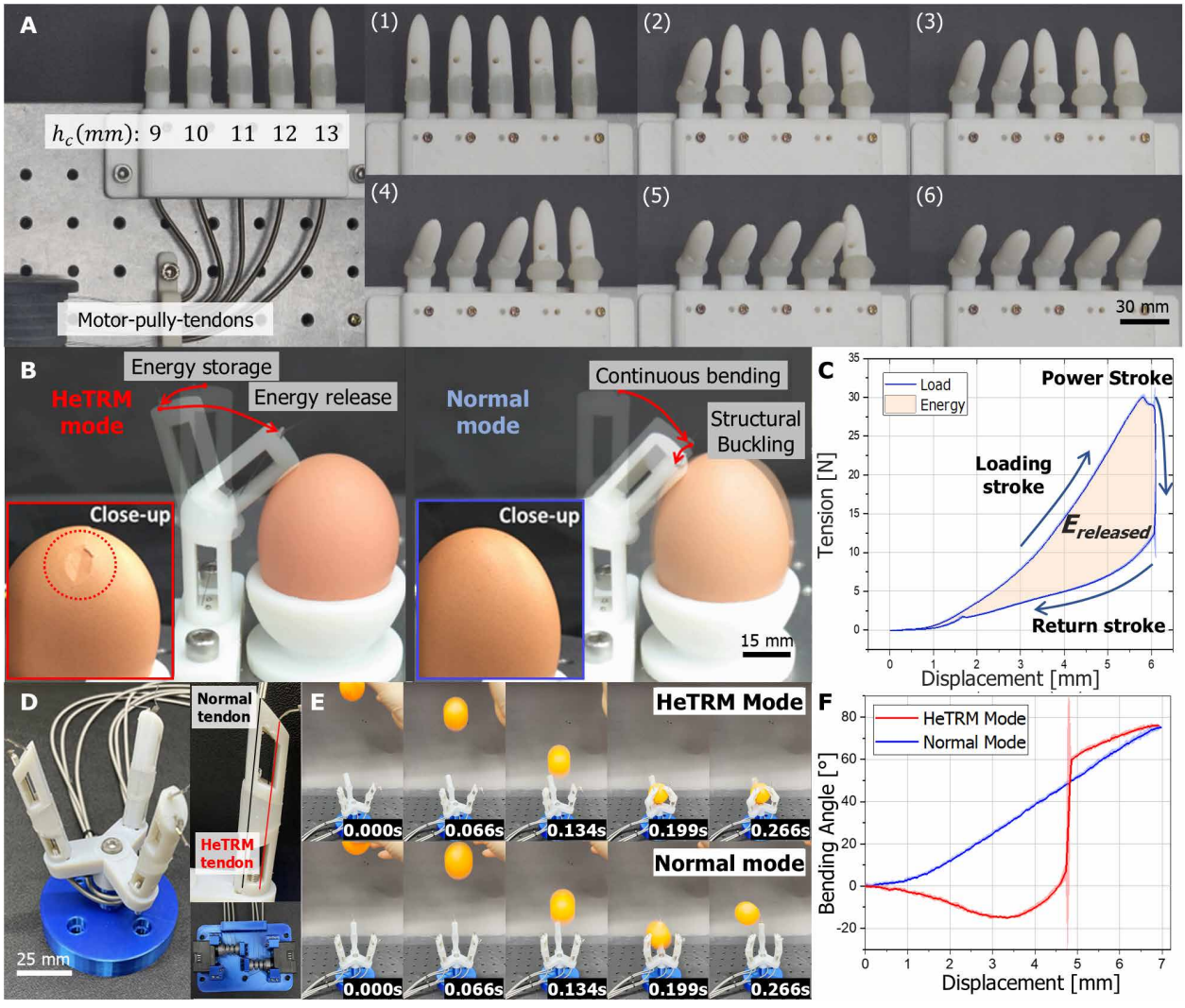

Fig. 3. HeTRM-based applications demonstrating preprogrammability, impulsive energy release, and rapid motion capabilities. (**A**) An artificial metachronal rhythm generated by five preprogrammed HeTRM beams arranged in a row with increasing h_C values (9 to 13 mm), driven by a single motor. Images (1) through (6) show the progression of snap-through actuation from left to right. (**B**) Comparison between HeTRM mode (left) and normal mode (right) through the eggshell-cracking challenge. The HeTRM mode efficiently cracked the eggshell through impulsive energy release, whereas the normal mode resulted in structural buckling without sufficient energy to crack the shell. (**C**) Displacement-force graph for the HeTRM eggshell cracker in the absence of external contact. The shaded closed area corresponds to the maximum energy released by the eggshell cracker. (**D**) Dual-mode soft gripper. The setup included two tendons for HeTRM and normal modes. (**E**) Time-lapse sequence showing the gripper's performance in catching a falling object (ping pong ball) using HeTRM mode (top row) and normal mode (bottom row). The HeTRM mode achieved a faster response because of impulsive actuation, successfully grasping the object. (**F**) The experimental result of the bending angle of the gripper as a function of tendon displacement for the HeTRM mode and the normal mode.

crack an eggshell (*47*). The eggshell-cracking challenge demonstrated that the HeTRM beam could temporarily achieve the same functionality as a powerful actuator through simple tendon displacement control. For example, replicating the HeTRM mode's impact with the normal mode would require a force-controlled actuator profile delivering 42.86 mJ within 0.03 s, with instantaneous energy release from rest.

Dual-mode HeTRM soft gripper

Many robotic devices, such as grippers, exoskeletons, and prosthetic hands, incorporate elements such as tendon-driven systems and flexible joints (*48*–*50*). This design strategy leverages advantages, such as adaptability, through underactuation of the tendon, a high degree of freedom in the joints, a lightweight design of the device body from the arrangement of the actuation and electronic components, and adequate precision. The driving speed of these devices, which is in a trade-off relationship with the output force, is determined by the rate at which the tendon is pulled. In essence, it is dictated by the configuration of the motor gearbox and the routing of the pulley-tendon system. Consequently, traditional devices have applied an adaptive high-speed mode or a high-force mode for the tendon-driven systems by actively or passively adjusting the effective gear ratio or the radius of the pulley (*51*–*53*).

To showcase the capability of the HeTRM in providing an additional design option to embody a high-speed swing in tendon-driven soft robotic bodies while also allowing for continuous bending, we developed a dual-mode soft gripper with three HeTRM beam–based fingers (Fig. 3, D and E). Similar to the HeTRM beam used in the egg-cracking challenge, the fingers of the developed gripper could perform either a normal mode, with continuous bending, or an HeTRM mode, with high-speed swing, by selectively pulling on two tendons located in each of the non-HeTRM and HeTRM paths (i.e., two tendons located at opposite ends of the slit-type tendon path). The experimental results for the behavior of the two modes, depicted in Fig. 3F, show that in the normal mode, the bending angle of the finger increased nonlinearly in response to the pulled distance of the tendon at an average rate of 3.8°/mm up to 1.3 mm, after which it increased almost linearly at a rate of 12.0°/mm. Consequently, when the tendon was pulled at a speed of 5 mm/s, as shown in movie S5, the normal mode bent at a maximum speed of 60.0°/s. In contrast, the HeTRM mode initially bent nonlinearly in the opposite direction, followed by an instantaneous swing at a speed of 56.1° in 0.066 s (i.e., 850°/s), which was more than 14 times faster than the normal mode. After the snap-through, the bending angle in the HeTRM mode was approximately 15° higher than that of the normal mode because of the kinematics of the tendons, which results in the HeTRM mode achieving a greater angle at the same displacement (fig. S7). However, as a trade-off for this rapid bending, the HeTRM mode required prestoring energy by pulling a critical distance of 4.69 mm, which took 0.938 s when pulled at 5 mm/s. This short preparation time suggested that the HeTRM mode may be less suitable for sudden, unexpected situations; however, we believe that it is advantageous in scenarios where the rapid motion is anticipated and can be strategically used.

The experimental results for the tip force of the finger against an object (load cell) located 16 mm horizontally from the tip showed identical tip force profiles at the same tension for both modes after contact (fig. S8A). The tension at which snap-through was triggered in the fingers was 9.5 N, and upon contact with the object, the tension dropped to 4.9 N. The maximum tip force resulting from the impact was 5.81 N (observed in a specific specimen, which was difficult to capture uniformly with a 100-Hz load cell) and then stabilized to 0.40 N.

By leveraging the ability to prepare for quick responses, the dual-mode gripper could instantly grasp a falling 2.7-g ping pong ball, as demonstrated in Fig. 3E and movie S5. The high speed and tension of the HeTRM power stroke were determined by the released energy, which was governed by the structural parameters, whereas the loading speed was still determined by the motor-tendon system design. This characteristic, which circumvents the traditional trade-off relationship, also enabled the gripper to stably and quickly catch a falling 70-g tangerine with a slow but sufficiently strong motor (movie S5) or to hold a 200-g mass (fig. S8B). Conversely, the normal bending mode, although more suitable for typical grasping scenarios, was unsuccessful in grasping either a falling ping pong ball or a falling tangerine. However, this normal bending mode could be selectively used for energy-efficient and convenient grasping of stationary objects.

Active triggering of HeTRM

Observing torque-reversal mechanisms in nature that facilitate controlled energy release (Fig. 1A) suggests that, to enable this function in HeTRMs, an additional trigger actuator would be required to apply torque in the opposite direction of the torque generated by the HeTRM tendon. A practical design option was to use the normal mode tendon of the dual-mode HeTRM as the triggering tendon. This tendon activated the normal mode when pulled from the neutral state, but when pulled while the HeTRM tendon was already engaged, it unbent the joint, shifting the HeTRM tendon toward the moment center and thereby triggering the snap-through behavior.

To explore the active energy-release function of the dual-mode HeTRM finger in detail, we conducted experiments where the HeTRM tendon was pulled to various displacements and then fixed, followed by pulling the triggering tendon (i.e., normal tendon) until the snap-through behavior was triggered. Afterward, the triggering tendon and the HeTRM tendon were sequentially relaxed. The displacement-tension results for the HeTRM tendon in Fig. 4A show that the active triggering paths labeled "a" to "h" follow the loading and return strokes of the self-triggered path (labeled "i," black line) at the corresponding displacements. The corresponding displacement-tension results for the triggering tendon are shown in Fig. 4B. As illustrated by the purple bars in Fig. 4C, the triggering energy gradually increased from labels "a" to "d" (HeTRM tendon displacement interval of 0.56 mm), then sharply decreased from labels "e" to "h" (HeTRM tendon displacement interval of 0.14 mm) and was no longer required for self-triggering. Figure 4C presents the results for total stored, released, and triggering energy (detailed numerical values are provided in table S5), demonstrating that active energy release could occur within a range lower than that of self-triggered energy release. Although the efficiency was lower for small energy releases, it became comparable to the maximum efficiency of self-triggered release above a certain threshold (label "e"). We expect that the active triggering mechanism of the HeTRM could potentially be used for controlled locomotion or precise and rapid swing of the dual-mode gripper fingers, with further research exploring the full potential of the dual-mode HeTRM.

HeTRM soft mechanical fuses for safe interaction

Although our study primarily explored the impulsive behavior of HeTRM, it is worth noting that its transient bistability could also be exploited for functional purposes. As shown in Fig. 5A, we developed a two-finger "safe" soft gripper that grasps objects through an initial bending induced by the HeTRM tendon (i.e., loading stroke); this design featured the snap-through bending direction of the fingers being the opposite of that in the dual-mode HeTRM soft gripper. In addition, the design parameters of the fingers were adjusted to increase both the snap-through displacement and the peak bending angle during the loading stroke (small α and large d_L, table S6). Accordingly, the bending during the loading stroke was directed toward gripping the object, whereas the snap-through behavior rapidly bent away from the object. This ensured that interaction with external objects occurred only at actuation levels below the critical point where the transient bistability ends, mechanically ceasing physical interaction at excessive actuation levels (Fig. 5B). Thus, like electrical fuses under overcurrent or shear pins under overload conditions, the HeTRM soft mechanical fuse physically ensured safety by preventing the transmission of unintended excessive inputs.

Figure 5C illustrates the experimental results of the force transmitted by a single HeTRM soft mechanical fuse to an object positioned at various horizontal distances (0, 2, 4, or 6 mm) as a function of tendon displacement. As the tendon was pulled, the tip force initially increased, reached a peak, and then decreased back to zero

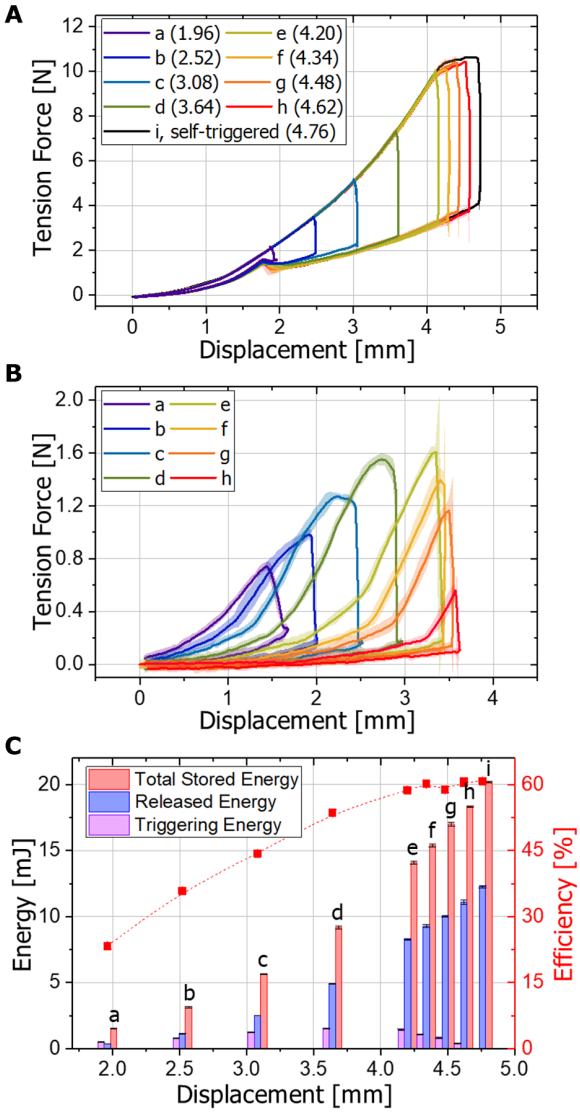

Fig. 4. Experimental analysis of tension force; displacement; and stored, released, and triggering energies for active triggering of the dual-mode HeTRM. (**A**) Force-displacement results during actively triggered paths (labeled a to h) and the self-triggered path (labeled i) for the HeTRM tendon and (**B**) the triggering tendon. The numbers in parentheses next to each label indicate the displacement (mm) of the HeTRM tendon. (**C**) Total stored energy, released energy, triggering energy, and efficiency for the active triggering. Specific numerical values are provided in table S5.

(for comparison, fig. S8 shows that the tip force of the dual-mode HeTRM soft gripper continued to increase with increasing input). Owing to the upper limit in force transmission, as demonstrated in movie S6 and Fig. 5A, the safe soft gripper bent its fingers in the opposite direction in the event of excessive input due to a control error, thereby releasing the object rather than inflicting damage. Consequently, it was capable of handling delicate objects, such as jelly, an origami box, a tomato, and cheese, without causing harm. The result further implied that the HeTRM soft mechanical fuse could potentially be applied in scenarios requiring safe human-robot interaction, where preventing unintended harm is critical.

HeTRM with three-dimensional out-of-plane motions

Helical configurations of soft continuum structures observed in natural systems, such as elephant trunks and snake bodies, have been effectively replicated in soft robotic designs, demonstrating substantial promise (*54*–*56*). Similarly, the HeTRM allowed for the connection of multiple joints in series, actuated by a single tendon, enabling not only large in-plane motion (Fig. 1C and fig. S4) but also three-dimensional (3D) out-of-plane motion through staggered configurations. We built a HeTRM twining tentacle composed of six HeTRM joints arranged in pairs, with each pair rotated by 22.5° relative to the next, as shown in Fig. 6A and movie S7. When the tendon was pulled, each joint was loaded and then underwent a synchronized snap-through motion, rapidly twining the HeTRM tentacle into a helical shape in 0.54 s. Moreover, we developed a HeTRM tentacle gripper, as shown in Fig. 6B and movie S7, which featured six HeTRM joints, with two proximal and four distal joints arranged at a 22.5° rotation relative to each other. The proximal joints ($d_L = 2.0$ mm) were designed to undergo snap-through before the distal joints ($d_L = 2.5$ mm), ensuring that the HeTRM tentacle gripper sequentially approached the cylindrical object (a paper roll) and then twined around it to securely grasp it.

We also investigated the generation of 3D motion using a single joint. As shown in Fig. 7A, the slit-type tendon path was positioned off center from the circular cross section. Our design aimed to place the moment center outside the tendon slit, causing the movement direction of the moment center to deviate with the tendon slit path. This also ensured that the bending shapes at both ends of the tendon path would exist in different planes when tension is applied. Torque reversal still occurred in this configuration: As the tendon was pulled, the moment center shifted and eventually crossed a virtual line perpendicular to the end of the slit. This action generated a lateral force that pulled the tendon to the opposite side. When this lateral force exceeded the static frictional force (proportional to the normal force acting on the wall), snap-through occurred, causing the tendon to slide along the slit (Fig. 7A, free-body diagram at "HeTRM occurs"). Consequently, this design enabled the generation of 3D out-of-plane motion simply by pulling and releasing the tendon, even with a single HeTRM joint. An example of the 3D spatial movement of the end tip of a single-jointed HeTRM is shown in Fig. 7B, with x, y, and z positions plotted in Fig. 7C and bending angle (θ) and orientation angle (φ) plotted in Fig. 7D. The end tip followed a trajectory resembling a bow or D shape when viewed from above. The HeTRM traced a curved path from one end of the bow's arc (loading stroke) until it reached a point beyond the center of the arc at which snap-through occurred, rapidly swinging the end tip to the opposite side. During the return stroke, the end tip followed a trajectory akin to the bowstring, returning to the origin.

This 3D spatial motion, combined with energy storage and release capabilities, was applied in a two-legged crawler designed to move by impacting the ground to propel itself forward (Fig. 7E and movie S8). The legs, designed to mimic a sea turtle's limbs, press down on the ground during the loading stroke, then swing back to propel the body forward during the power stroke. The 3D motion design of the return stroke, where the legs lift off the ground before returning to the initial position, was intended to mitigate the difficulty of returning to the initial shape when external forces, such as friction from the ground, were applied. The ability to exert a high force enabled the crawler to move forward not only on rigid

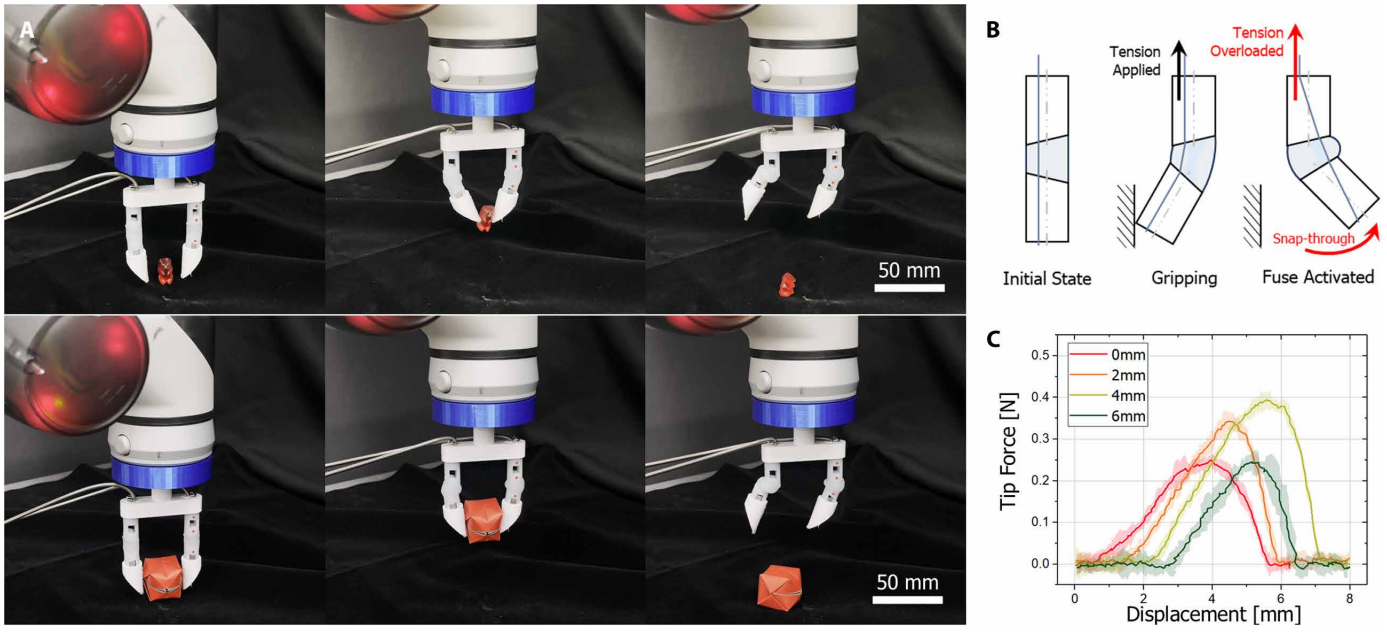

Fig. 5. HeTRM soft gripper with embodied mechanical fuse function. (**A**) The gripper delicately handled a piece of jelly (top) and an origami box (bottom), demonstrating its capability to release the object without causing damage in response to excessive actuation caused by control errors. (**B**) Schematic representation of the HeTRM soft mechanical fuse mechanism, illustrating the transition from the initial state to gripping mode and the snap-through behavior that activates the fuse under excessive tension or displacement. (**C**) Experimental results showing the force transmitted by a single HeTRM soft mechanical fuse to an object.

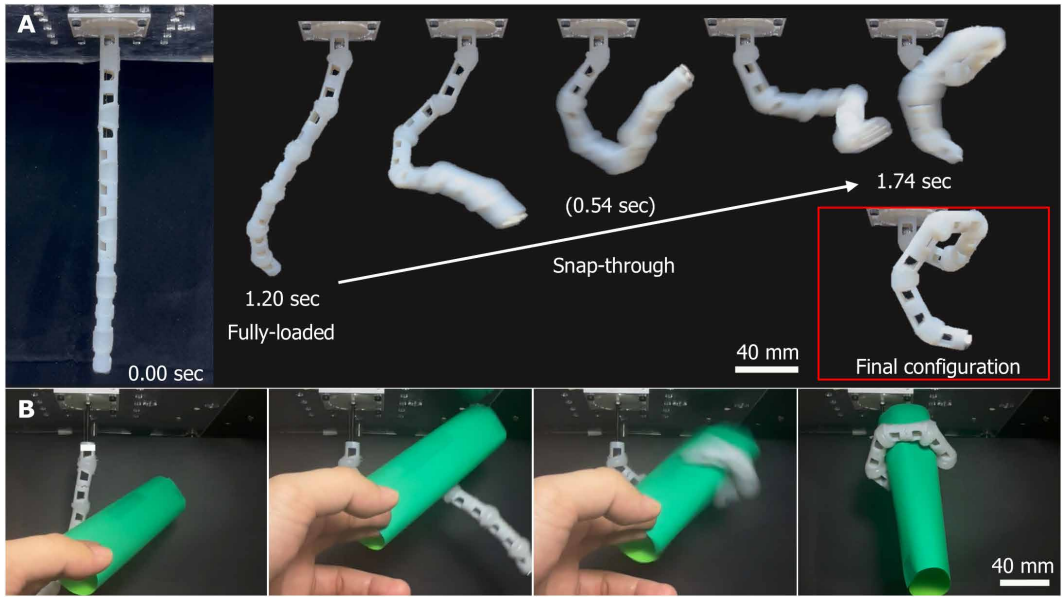

Fig. 6. HeTRM twining tentacles with serial and rotational connection of joints. (**A**) The HeTRM twining tentacle consists of six HeTRM joints arranged in pairs of two, each pair arranged at a 22.5° rotation relative to each other. The snap-through behaviors were designed to trigger simultaneously, generating a rapid twining motion. (**B**) The HeTRM tentacle gripper twining around a cylindrical object. The gripper features six HeTRM joints, with two proximal and four distal pairs arranged at a 22.5° rotation.

surfaces but also on uneven, wet sand with low ground reaction force (Fig. 7F and movie S8).

DISCUSSION

Although bistable structures and torque-reversal mechanisms share the ability to store and release energy through snap-through motion, they can be distinctively used in that bistable structures generally use internal stress, whereas torque-reversal mechanisms use controlled compression force. The torque-reversal mechanism was previously designed using a latching mechanism and an n-bar linkage. In this work, we presented the torque-reversal mechanism for soft robotics with hyperelastic soft joints, drawing inspiration from the stability switching of soft-bodied cilia. We found that the

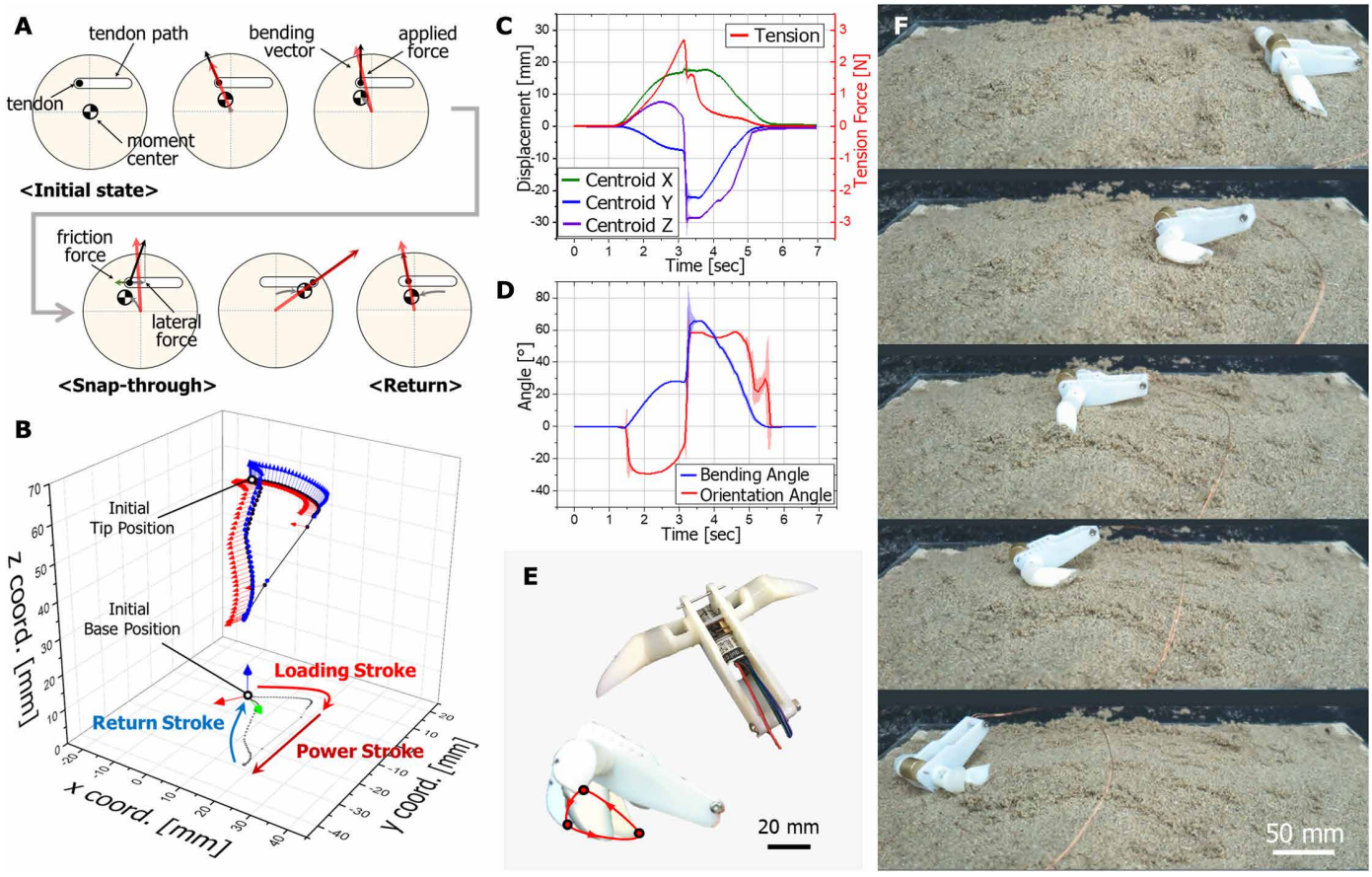

Fig. 7. HeTRM for the out-of-plane spatial motion. (**A**) Schematic illustration of the 3D HeTRM showing the off-center slit-type tendon path. The changing direction of force in the HeTRM joint generated the out-of-plane 3D motion. (**B**) Motion capture result for a single-joint HeTRM beam with out-of-plane spatial motion. (**C**) Displacement of the end tip in *x*, *y*, and *z* coordinates and corresponding tension force over time during the motion cycle. (**D**) Bending angle (θ) and orientation angle (φ) of the 3D HeTRM plotted against time. (**E**) The two-legged soft crawler with two 3D HeTRM legs. (**F**) The crawler moving on wet sand, demonstrating its capability to traverse uneven terrain.

core principle governing the HeTRM is that, in contrast with bistable structures that invariably have two stable points, it exhibits transient bistability under compression but becomes monostable under certain conditions where a snap-through occurs. We investigated the compression-responsive transient bistability of HeTRM by modeling and experiments and its engineering features, including energy storage and release for both self-triggering and active triggering, dual-mode actuation, mechanical safety mechanism, and 3D motions. Although this study introduces the concept of the HeTRM and broadly explores its potential functionalities, further research is needed to enhance its scalability and applicability. For instance, incorporating shear stress into the modeling process would increase precision. More generalized approaches, such as finite element methods (FEMs), could provide greater scalability for out-of-plane 3D motion and multijoint systems. However, challenges remain in achieving convergence in FEM simulations under conditions of large compressive deformation and transient motion. In addition, to expand the utility of this mechanism, further research is needed to explore its implementation and functionality across a broader range of scales. We believe that the HeTRM holds promise as a soft robotic component capable of producing impulsive motion or controlled bistability, and we also hope that our approach offers a fresh perspective on the design of soft structures using snap-through instabilities.

MATERIALS AND METHODS

Fabrication of the HeTRM

The fabrication process, which involved 3D printing and silicone molding, is illustrated in fig. S9. Rigid segments and molds (VeroWhite, Stratasys) were printed using a high-resolution 3D printer (Connex 260, Stratasys). The mold consisted of two parts, top and bottom. The rigid segments were fixed at a predetermined distance within the bottom mold to define the length of the soft segment. To create the slit-type tendon path, a slit mold was inserted between the rigid segments. These slit molds were fabricated by laser-cutting acrylic sheets. After fixation, silicone (Ecoflex 00-30, Smooth-On, Inc.) was first poured into the bottom mold. The top mold had holes corresponding to the cavities for the soft segments. The top mold was then placed over the bottom mold, and silicone was poured again through these holes. After curing for more than 3 hours in an oven at 65°C, the molds and the plate were removed. To ensure robust bonding between the rigid segments and the soft joints, silicone adhesive (Sil-Poxy, Smooth-On, Inc.) was applied to the joint edges. A kink-free

titanium wire (Beadalon) was used as the tendon to actuate the joint, with the tendon fixed and tensioned. Teflon grease was applied to reduce friction between the tendon and the elastomer. For the experiment, 3D-printed markers (Prusament PLA, Prusa or TangoBlack, Stratasys) were either engraved or attached along the longitudinal direction of the rigid segments for image tracking.

Experimental setups for the characterization of the HeTRM

The experimental setups for in-plane motion, out-of-plane motion, and image analysis are shown in fig. S10. Each sample was mounted vertically onto a setup, with the joint positioned to ensure that the tendon passed through the slit along the designated path and connected to a motor (Dynamixel XC430-T240BB-T, Robotis). The 3D-printed joint's mount and load cell mount were designed to allow fine adjustment of their position. This facilitated the setup of a desired predefined offset of the tendon path from the joint center, as well as the distance between the joint and the load cell. Once secured, the tendon was pulled by the motor at a constant speed. To measure the tendon force, a three-pulley tension measurement system with a load cell (BCL Loadcell, CAS) was used to measure tension, where the tendon pressed down on the pulley above the load cell at an angle of 120°. The resulting force on the load cell could be calculated as two times the tendon force multiplied by the cosine of 60°, which simplifies to a force equal to the tendon force.

Characterization of the hyperelasticity of the soft materials

To determine the hyperelastic characteristics of Ecoflex 00-30 for use in soft joints, a compression test was conducted (fig. S2). This was because the HeTRM is driven by compressive loads, requiring material data for modeling under negative strain conditions. A cylindrical specimen, 10 mm in diameter and 10 mm in height, was fabricated to match the scale of the joint. The specimen's top and bottom surfaces were secured at the base of the tensile testing machine to ensure zero-displacement conditions. The compression test was performed at a rate of 1 mm/s using the RB 302 ML universal testing machine (R&B Co. Ltd). The experimental data were analyzed and curve fitted using the Yeoh model (*57*).

Image analysis of the 2D bending of the HeTRM

Image analysis was used to evaluate the flexion of the joint. For the image analysis, 3D-printed markers (Prusament PLA, Prusa or TangoBlack, Stratasys) were either engraved or attached along the longitudinal direction of the rigid segments for image tracking. A camera (StreamCam, Logitech) capturing at 30 frames per second was mounted perpendicular to the joint to record joints' motion. Markers imprinted on the sides of the joint were detected, and their centers were computed with image-processing libraries in MATLAB and Python. The flexion angle was calculated on the basis of the relative angular difference between the two rigid segments, with each segment's angle determined using the fixed positions of two markers on the segment. This analysis was conducted while the joint underwent cyclic loading and release during a single motion cycle.

3D motion tracking analysis of the HeTRM's out-of-plane spatial motion

3D motion tracking analysis was conducted to examine the 3D movement of the joint using a total of six markers, three each on the basal and distal ends. On each side of the joint, three markers were arranged in a triangular configuration to define a plane. Motion tracking was performed using five OptiTrack devices (Primex 13W, OptiTrack), capturing the cyclic behavior of the joint through repetitive loading and release of the tendon. The joint motion was analyzed on the basis of the displacement and angle between the centers of the basal plane and the distal plane.

Design considerations for the demonstrations

To demonstrate the HeTRM artificial metachronal rhythm, five HeTRM joints were arranged in parallel at regular intervals, with the tendons routed through Bowden cables and synchronized by a single pulley for joint actuation. Although the snap-through displacement changed nonlinearly with design parameters α and d_L, it changed linearly with h_C. Therefore, continuous triggering could be achieved by simply designing h_C values with narrow and constant intervals (fig. S6 and table S6).

For the eggshell cracker, the joints should be designed with a low α and high h_C, d_L, and d_R values to maximize energy release with a fixed radius. We increased the energy-release capacity by adjusting the slit-path design parameters, intentionally designing the joints with high d_L and d_R values to enable a large amount of energy release from the joint (table S6). The eggs were positioned on an eggcup-shaped support, 37.5 mm away from the joint.

For the dual-mode HeTRM gripper, it was advisable to reduce the snap-through displacement to quickly recharge the power stroke. This could be achieved by increasing α or decreasing d_L. However, because d_L was excessively sensitive to manufacturing errors at small values (Fig. 2I), we determined that increasing α was a better approach (table S6). The three fingers, each with a total length of 60 mm, were spaced 21.32 mm apart from the center of the base. To facilitate gripping, the joints were attached at an angle of 12.5° relative to the gripper axis. The tendons driving the three joints were controlled separately on the basis of the operation mode, either HeTRM mode or normal mode. In this experiment, two motors were used to drive each mode; however, it would be also possible to design a system using a clutch mechanism, enabling control of both movements with a single motor (*58*).

The mechanical fuse gripper was designed to increase the snap-through displacement to expand the effective gripping area and achieve more gradual bending stiffness in the gripping region. Therefore, we intentionally designed it with small α and large d_L parameters (table S6). The joints were mounted on the base with 50-mm spacing.

For the twining tentacle, the joints connected in series were each 3D-printed, but the rigid segments were designed to interlock at a sawtooth angle of 22.5° for assembly. The tendon was realigned within the rigid segments between the joints, ensuring that the initial position was at the end of each slit. The differentiation of critical displacements for sequential triggering was implemented through differences in d_L design values (2.0 and 2.5 mm, table S6).

For the crawler with 3D motion, the joint ends were designed to be wide (large d_L and d_R, table S6) so that after contacting the ground during the loading stroke, the power stroke could push against the ground. The two arms were attached to the base component, and a 6-V geared motor with a 10-mm-diameter pulley was installed to enable simultaneous pulling of both arms.

A long box-shaped HeTRM joint

In the main text, we focused on discussing the cylindrical (cylinder-shaped) HeTRM joint. However, the core principle of HeTRM

technology is not limited to a specific shape but has the potential to be applied to various forms of bending soft joints. As an example, as shown in fig. S11, a long box-shaped joint can also exhibit the HeTRM behavior (table S6).

Statistical analysis

All measurements were repeated for at least three specimens, with five tests conducted per specimen. During each experiment, tendon displacement, tension force, and the joint's flexion angle were recorded over time. The average values and SDs were then computed, and all graphs and tables present error bars corresponding to two times the SD, equivalent to a 95% confidence interval.

Supplementary Materials

The PDF file includes:

Methods
Tables S1 to S6
Figs. S1 to S11
Legends for movies S1 to S8

Other Supplementary Material for this manuscript includes the following:

Movies S1 to S8

REFERENCES AND NOTES

1. S.-M. Baek, S. Yim, S.-H. Chae, D.-Y. Lee, K.-J. Cho, Ladybird beetle-inspired compliant origami. *Sci. Robot.* **5**, eaaz6262 (2020).
2. E. W. Hawkes, C. Xiao, R.-A. Peloquin, C. Keeley, M. R. Begley, M. T. Pope, G. Niemeyer, Engineered jumpers overcome biological limits via work multiplication. *Nature* **604**, 657–661 (2022).
3. E. W. Hawkes, L. H. Blumenschein, J. D. Greer, A. M. Okamura, A soft robot that navigates its environment through growth. *Sci. Robot.* **2**, eaan3028 (2017).
4. W. Kim, J. Eom, K.-J. Cho, A dual-origami design that enables the quasisequential deployment and bending motion of soft robots and grippers. *Adv. Intell. Syst.* **4**, 2100176 (2022).
5. M. A. Robertson, J. Paik, New soft robots really suck: Vacuum-powered systems empower diverse capabilities. *Sci. Robot.* **2**, eaan6357 (2017).
6. O. Bliah, S. Joe, R. Reinberg, A. B. Nardin, L. Beccai, S. Magdassi, 3D printing stretchable and compressible porous structures by polymerizable emulsions for soft robotics. *Mater. Horiz.* **10**, 4976–4985 (2023).
7. W. Kim, J. Byun, J.-K. Kim, W.-Y. Choi, K. Jakobsen, J. Jakobsen, D.-Y. Lee, K.-J. Cho, Bioinspired dual-morphing stretchable origami. *Sci. Robot.* **4**, eaay3493 (2019).
8. M. Taghavi, T. Helps, J. Rossiter, Electro-ribbon actuators and electro-origami robots. *Sci. Robot.* **3**, eaau9795 (2018).
9. M. Duduta, E. Hajiesmaili, H. Zhao, R. J. Wood, D. R. Clarke, Realizing the potential of dielectric elastomer artificial muscles. *Proc. Natl. Acad. Sci. U.S.A.* **116**, 2476–2481 (2019).
10. W. Pang, S. Xu, J. Wu, R. Bo, T. Jin, Y. Xiao, Z. Liu, F. Zhang, X. Cheng, K. Bai, H. Song, Z. Xue, L. Wen, Y. Zhang, A soft microrobot with highly deformable 3D actuators for climbing and transitioning complex surfaces. *Proc. Natl. Acad. Sci. U.S.A.* **119**, e2215028119 (2022).
11. G. Z. Lum, Z. Ye, X. Dong, H. Marvi, O. Erin, W. Hu, M. Sitti, Shape-programmable magnetic soft matter. *Proc. Natl. Acad. Sci. U.S.A.* **113**, E6007–E6015 (2016).
12. H. Gu, Q. Boehler, H. Cui, E. Secchi, G. Savorana, C. De Marco, S. Gervasoni, Q. Peyron, T.-Y. Huang, S. Pane, A. M. Hirt, D. Ahmed, B. J. Nelson, Magnetic cilia carpets with programmable metachronal waves. *Nat. Commun.* **11**, 2637 (2020).
13. J. Byun, M. Park, S.-M. Baek, J. Yoon, W. Kim, B. Lee, Y. Hong, K.-J. Cho, Underwater maneuvering of robotic sheets through buoyancy-mediated active flutter. *Sci. Robot.* **6**, (2021).
14. S. Deglurkar, C. Xiao, L. Gockowski, M. T. Valentine, E. W. Hawkes, A light- and heat-seeking vine-inspired robot with material-level responsiveness. *IEEE Robot. Autom. Lett.* **9**, 1–8 (2024).
15. L. Cecchini, S. Mariani, M. Ronzan, A. Mondini, N. M. Pugno, B. Mazzolai, 4D printing of humidity-driven seed inspired soft robots. *Adv. Sci.* **10**, (2023).
16. C. A. Aubin, R. H. Heisser, O. Peretz, J. Timko, J. Lo, E. F. Helbling, S. Sobhani, A. D. Gat, R. F. Shepherd, Powerful, soft combustion actuators for insect-scale robots. *Science* **381**, 1212–1217 (2023).
17. N. W. Bartlett, M. T. Tolley, J. T. B. Overvelde, J. C. Weaver, B. Mosadegh, K. Bertoldi, G. M. Whitesides, R. J. Wood, A 3D-printed, functionally graded soft robot powered by combustion. *Science* **349**, 161–165 (2015).
18. H. Zhou, S. Cao, S. Zhang, F. Li, N. Ma, Design of a fuel explosion-based chameleon-like soft robot aided by the comprehensive dynamic model. *Cyborg Bionic Syst.* **4**, (2023).
19. Z. Yoder, D. Macari, G. Kleinwaks, I. Schmidt, E. Acome, C. Keplinger, A soft, fast and versatile electrohydraulic gripper with capacitive object size detection. *Adv. Funct. Mater.* **33**, 2209080 (2023).
20. N. Kellaris, P. Rothemund, Y. Zeng, S. K. Mitchell, G. M. Smith, K. Jayaram, C. Keplinger, Spider-inspired electrohydraulic actuators for fast, soft-actuated joints. *Adv. Sci.* **8**, e2100916 (2021).
21. Y. Chi, Y. Li, Y. Zhao, Y. Hong, Y. Tang, J. Yin, Bistable and multistable actuators for soft robots: Structures, materials, and functionalities. *Adv. Mater.* **34**, 2110384 (2022).
22. A. Pal, V. Restrepo, D. Goswami, R. V. Martinez, Exploiting mechanical instabilities in soft robotics: Control, sensing, and actuation. *Adv. Mater.* **33**, 2006939 (2021).
23. Y. Cao, M. Derakhshani, Y. Fang, G. Huang, C. Cao, Bistable structures for advanced functional systems. *Adv. Funct. Mater.* **31**, 2106231 (2021).
24. J. T. B. Overvelde, T. Kloek, J. J. A. D'haen, K. Bertoldi, Amplifying the response of soft actuators by harnessing snap-through instabilities. *Proc. Natl. Acad. Sci. U.S.A.* **112**, 10863–10868 (2015).
25. R. Baumgartner, A. Kogler, J. M. Stadlbauer, C. C. Foo, R. Kaltseis, M. Baumgartner, G. Mao, C. Keplinger, S. J. A. Koh, N. Arnold, Z. Suo, M. Kaltenbrunner, S. Bauer, A lesson from plants: High-speed soft robotic actuators. *Adv. Sci.* **7**, (2020).
26. C. Keplinger, T. Li, R. Baumgartner, Z. Suo, S. Bauer, Harnessing snap-through instability in soft dielectrics to achieve giant voltage-triggered deformation. *Soft Matter* **8**, 285–288 (2012).
27. B. Gorissen, D. Melancon, N. Vasios, M. Torbati, K. Bertoldi, Inflatable soft jumper inspired by shell snapping. *Sci. Robot.* **5**, eabb1967 (2020).
28. Y. Tang, Y. Chi, J. Sun, T.-H. Huang, O. H. Maghsoudi, A. Spence, J. Zhao, H. Su, J. Yin, Leveraging elastic instabilities for amplified performance: Spine-inspired high-speed and high-force soft robots. *Sci. Adv.* **6**, eaaz6912 (2020).
29. D. K. Patel, X. Huang, Y. Luo, M. Mungekar, M. K. Jawed, L. Yao, C. Majidi, Highly dynamic bistable soft actuator for reconfigurable multimodal soft robots. *Adv. Mater. Technol.* **8**, 2201259 (2023).
30. Y. Chi, Y. Hong, Y. Zhao, Y. Li, J. Yin, Snapping for high-speed and high-efficient butterfly stroke–like soft swimmer. *Sci. Adv.* **8**, eadd3788 (2022).
31. T. Chen, O. R. Bilal, K. Shea, C. Daraio, Harnessing bistability for directional propulsion of soft, untethered robots. *Proc. Natl. Acad. Sci. U.S.A.* **115**, 5698–5702 (2018).
32. Y. Forterre, J. M. Skotheim, J. Dumais, L. Mahadevan, How the Venus flytrap snaps. *Nature* **433**, 421–425 (2005).
33. Z. Zhang, X. Ni, H. Wu, M. Sun, G. Bao, H. Wu, S. Jiang, Pneumatically actuated soft gripper with bistable structures. *Soft Robot.* **9**, 57–71 (2022).
34. S.-W. Kim, J.-S. Koh, J.-G. Lee, J. Ryu, M. Cho, K.-J. Cho, Flytrap-inspired robot using structurally integrated actuation based on bistability and a developable surface. *Bioinspir. Biomim.* **9**, 036004 (2014).
35. Z. Zhang, X. Li, X. Yu, H. Chai, Y. Li, H. Wu, S. Jiang, Magnetic actuation bionic robotic gripper with bistable morphing structure. *Compos. Struct.* **229**, 111422 (2019).
36. P. Rothemund, A. Ainla, L. Belding, D. J. Preston, S. Kurihara, Z. Suo, G. M. Whitesides, A soft, bistable valve for autonomous control of soft actuators. *Sci. Robot.* **3**, eaar7986 (2018).
37. X. Zhang, Y. Wang, Z. Tian, M. Samri, K. Moh, R. M. McMeeking, R. Hensel, E. Arzt, A bioinspired snap-through metastructure for manipulating micro-objects. *Sci. Adv.* **8**, eadd4768 (2022).
38. Z. Chen, Q. Guo, C. Majidi, W. Chen, D. J. Srolovitz, M. P. Haataja, Nonlinear geometric effects in mechanical bistable morphing structures. *Phys. Rev. Lett.* **109**, 114302 (2012).
39. N. Vasios, B. Deng, B. Gorissen, K. Bertoldi, Universally bistable shells with nonzero Gaussian curvature for two-way transition waves. *Nat. Commun.* **12**, 695 (2021).
40. J.-S. Koh, S.-P. Jung, M. Noh, S.-W. Kim, K.-J. Cho, Flea inspired catapult mechanism with active energy storage and release for small scale jumping robot, in *2013 IEEE International Conference on Robotics and Automation* (IEEE, 2013), pp. 26–31.
41. J.-S. Koh, E. Yang, G.-P. Jung, S.-P. Jung, J. H. Son, S.-I. Lee, P. G. Jablonski, R. J. Wood, H.-Y. Kim, K.-J. Cho, Jumping on water: Surface tension–dominated jumping of water striders and robotic insects. *Science* **349**, 517–521 (2015).
42. T. Kaji, A. Anker, C. S. Wirkner, A. R. Palmer, Parallel saltational evolution of ultrafast movements in snapping shrimp claws. *Curr. Biol.* **28**, 106–113.e4 (2018).
43. S. J. Longo, R. St. Pierre, S. Bergbreiter, S. Cox, B. Schelling, S. N. Patek, Geometric latches enable tuning of ultrafast, spring-propelled movements. *J. Exp. Biol.* **226**, jeb244363 (2023).
44. E. Steinhardt, N. P. Hyun, J. Koh, G. Freeburn, M. H. Rosen, F. Z. Temel, S. N. Patek, R. J. Wood, A physical model of mantis shrimp for exploring the dynamics of ultrafast systems. *Proc. Natl. Acad. Sci. U.S.A.* **118**, (2021).
45. T. J. Mitchison, H. M. Mitchison, How cilia beat. *Nature* **463**, 308–309 (2010).
46. J. Elgeti, G. Gompper, Emergence of metachronal waves in cilia arrays. *Proc. Natl. Acad. Sci. U.S.A.* **110**, 4470–4475 (2013).

47. P. T. Chou, J. L. Lin, A study of impact energy on eggshell crack. *IOP Conf. Ser. Mater. Sci. Eng.* **378**, 012010 (2018).
48. H. In, B. B. Kang, M. Sin, K.-J. Cho, Exo-Glove: A wearable robot for the hand with a soft tendon routing system. *IEEE Robot. Autom. Mag.* **22**, 97–105 (2015).
49. Y. Li, Y. Chen, T. Ren, Y. Hu, H. Liu, S. Lin, Y. Yang, Y. Li, J. Zhou, A dual-mode actuator for soft robotic hand. *IEEE Robot. Autom. Lett.* **6**, 1144–1151 (2021).
50. Y. Zhang, W. Zhang, J. Yang, W. Pu, Bioinspired soft robotic fingers with sequential motion based on tendon-driven mechanisms. *Soft Robot.* **9**, 531–541 (2022).
51. K. W. O'Brien, A. Xu, D. J. Levine, C. A. Aubin, H.-J. Yang, M. F. Xiao, L. W. Wiesner, R. F. Shepherd, Elastomeric passive transmission for autonomous force-velocity adaptation applied to 3D-printed prosthetics. *Sci. Robot.* **3**, eaau5543 (2018).
52. Y. J. Shin, H. J. Lee, K.-S. Kim, S. Kim, A robot finger design using a dual-mode twisting mechanism to achieve high-speed motion and large grasping force. *IEEE Trans. Robot.* **28**, 1398–1405 (2012).
53. J. T. Belter, A. M. Dollar, A passively adaptive rotary-to-linear continuously variable transmission. *IEEE Trans. Robot.* **30**, 1148–1160 (2014).
54. L. H. Blumenschein, N. S. Usevitch, B. H. Do, E. W. Hawkes, A. M. Okamura, Helical actuation on a soft inflated robot body, in *2018 IEEE International Conference on Soft Robotics (RoboSoft)* (IEEE, 2018), pp. 245–252.
55. Q. Guan, J. Sun, Y. Liu, N. M. Wereley, J. Leng, Novel bending and helical extensile/contractile pneumatic artificial muscles inspired by elephant trunk. *Soft Robot.* **7**, 597–614 (2020).
56. B. Liao, H. Zang, M. Chen, Y. Wang, X. Lang, N. Zhu, Z. Yang, Y. Yi, Soft rod-climbing robot inspired by winding locomotion of snake. *Soft Robot.* **7**, 500–511 (2020).
57. O. H. Yeoh, Some forms of the strain energy function for rubber. *Rubber Chem. Technol.* **66**, 754–771 (1993).
58. K. J. Cho, G. P. Jung, S. P. Jung, G. P. Jung, Active clutch mechanism and hopping robot having same, U.S. Patent US10724507B2 (2020).

Acknowledgments

Funding: This research was supported by the National Research Foundation of Korea (NRF) funded by the Korean government (MSIT) (grant RS-2023-00208052) (to K.-J.C.) and the Korea Institute of Science and Technology (Institutional Program grant 2E33004) (to W.K.).

Author contributions: Conceptualization: W.-Y.C., W.K., and Y.-J.P.; methodology: W.-Y.C. and W.K.; investigation: W.-Y.C., W.K., J.-R.C., S.Y.Y., and S.M.; visualization: W.-Y.C., W.K., J.-R.C., S.Y.Y., and S.M.; funding acquisition: W.K. and K.-J.C.; project administration: K.-J.C.; supervision: Y.-J.P. and K.-J.C.; writing–original draft: W.-Y.C. and W.K.; writing–review and editing: W.-Y.C., W.K., J.-R.C., S.Y.Y., Y.-J.P., and K.-J.C. **Competing interests:** The authors declare that they have no competing interests. **Data and materials availability:** Codes for the HeTRM snap-through modeling have been deposited in Dryad at https://doi.org/10.5061/dryad.kh18932h6. All remaining data are available in the paper or the Supplementary Materials.

Submitted 20 February 2024
Accepted 23 December 2024
Published 29 January 2025
10.1126/scirobotics.ado7696